

# A Multiresolution Ensemble Kalman Filter using Wavelet Decomposition.

Kyle S. Hickmann,<sup>\*</sup> Humberto C. Godinez<sup>†</sup>

## Abstract

We present a method of using classical wavelet based multiresolution analysis to separate scales in model and observations during data assimilation with the ensemble Kalman filter. In many applications, the underlying physics of a phenomena involve the interaction of features at multiple scales. Blending of observational and model error across scales can result in large forecast inaccuracies since large errors at one scale are interpreted as inexact data at all scales. Our method uses a transformation of the observation operator in order to separate the information from different scales of the observations. This naturally induces a transformation of the observation covariance and we put forward several algorithms to efficiently compute the transformed covariance. Another advantage of our multiresolution ensemble Kalman filter is that scales can be weighted independently to adjust each scale's effect on the forecast. To demonstrate feasibility we present applications to a one dimensional Kuramoto-Sivashinsky (K-S) model with scale dependent observation noise and an application involving the forecasting of solar photospheric flux. The latter example demonstrates the multiresolution ensemble Kalman filter's ability to account for scale dependent model error. Modeling of photospheric magnetic flux transport is accomplished by the Air Force Data Assimilative Photospheric Transport (ADAPT) model.

**Keywords:** data assimilation, wavelets, multiresolution analysis, ensemble Kalman filter

## 1 Introduction

Combining large-scale physics simulations with data to generate informed forecasts, with quantified uncertainty, is a common task in modern science [15, 25, 40]. A prevalent method to accomplish this task is the ensemble Kalman filter (EnKF) [24] which can provide a forecast of the mean behavior of the system along with confidence intervals. The EnKF assumes that both the model and observations have a Gaussian probability distribution. Additionally, it is frequently assumed that model and observation covariance matrices are diagonal or block diagonal, implying that errors associated with different state variables are

---

<sup>\*</sup>Applied Mathematics and Plasma Physics, Los Alamos National Laboratory, hickmank@lanl.gov

<sup>†</sup>Applied Mathematics and Plasma Physics, Los Alamos National Laboratory, hgodinez@lanl.gov

<sup>0</sup>2010 MSC:

uncorrelated or weakly correlated. These types of assumptions are even more prevalent when variables or observations are far apart in space and/or time [34]. However, if observation or model errors are scale dependent, correlations of errors between variables may not be known *a priori* and discarding some of these correlations artificially can cause ensemble collapse resulting in large forecast errors.

The problem of scale dependent observation and model error in forecasting can be seen in atmospheric data assimilation where models that do a good job of forecasting large scale phenomenon are coupled with models of small scale turbulent effects [12, 13, 30, 54]. Here we propose to address the scale dependence problem in the EnKF by using a multiresolution analysis (MRA). Wavelet based MRA has been used to analyze the statistical properties of weather models and ocean models in the past [9, 10, 11, 13, 17, 41]. However, this has usually been done retrospectively. Here we propose to use the results of MRA scale separation during the generation of a data assimilative forecast by directly coupling the MRA with the EnKF.

Wavelet analysis has been applied to the EnKF in the past [9, 11, 17]. Previously MRA was used to offer a more accurate approximation to the ensemble covariance. Past work first transformed the ensemble to the wavelet domain where a diagonal wavelet covariance was estimated, before assimilation was performed, the wavelet covariance was then transformed back to the original model domain. Approximating the covariance in this way offers a more accurate estimation of the ensemble covariance due to a regularization effect that the wavelet transform naturally provides. However, the improvement in this approximation relies on the assumption that the wavelet transform approximately diagonalizes the ensemble covariance, which is not always the case [19, 50].

Here, we apply the wavelet transform to the observation operator directly. The transformation to the wavelet domain is computed only once during assimilation as a preprocessing step and the inverse transformation is never computed. Using the wavelet transform to modify the observation operator, instead of modifying the ensemble covariance, has the effect of offering a computationally efficient, scale dependent, extension of the EnKF. We also show that an iterative application of the EnKF with a scale dependent observation operator allows for propagation of information between scales. Thereby eliminating the need for assumptions about independence of scales. Another advantage of our method is that, once the transformation to the wavelet domain has been computed, it is natural to use an ensemble inflation coefficient to assign trust to the observations and model error based on *a priori* knowledge about the accuracy of observations and model at each scale.

We demonstrate our methods on two different models. First, we apply the multiresolution EnKF (MrEnKF) to the Kuramoto-Sivashinsky (K-S) equation. The K-S equation is a 1D nonlinear partial differential evolution equation which possesses multi-scale dynamics. The K-S equation is used here to demonstrate the advantage of the MrEnKF in a data assimilation experiment in which we assign varying degrees of observational noise to distinct wavelet scales. It is assumed that the large scales are observed more accurately than the finer scales. Since the large scales contain more information about the unstable low Fourier modes, this observation experiment demonstrates the advantages of the MrEnKF over the scale independent EnKF when dealing with multi-scale models.

The second example we present involves forecasting the magnetic flux transported across

the solar photosphere. Our application is the Air Force Data Assimilative Photospheric Transport (ADAPT) model of photospheric flux propagation [5, 6, 7, 33], a collaborative modeling and forecasting effort between Los Alamos National Laboratory and the Air Force Research Laboratory in Kirkland ABQ. The solar photosphere application highlights the challenges encountered in realistic modeling and forecasting efforts within the science community. Many scientist are interested in the tracking of emergent coherent regions of magnetic flux. These large clumps of magnetic flux are known as *active regions* and are primary drivers of large space weather events such as Coronal Mass Ejections (CMEs) [4, 27, 28, 52]. When implementing a standard EnKF, the active regions tend to diffuse and lose structure after only one assimilation cycle. By the end of the assimilation window, it is difficult to maintain a coherent active region structure with the EnKF. On the other hand, we show that the MrEnKF performs much better in regards to maintaining a coherent active region, since the MrEnKF assigns greater confidence to observations characteristics at the scale of active regions. Once the structure is preserved for a newly emerging active region, successive observations of the active region allow for increasing definition in ADAPT’s data assimilation mechanism.

In section 2 we quickly review the classical wavelet multiresolution analysis, set up notation, and point the interested reader to references on wavelet analysis. Section 3 then gives a derivation of our multiresolution ensemble Kalman Filter scheme. In section 4 we discuss ways to approximate the change to the observation covariance when using the wavelet transformation in a computationally efficient manner. Section 5 details the role of ensemble inflation in the multiresolution EnKF. Our examples using the Kuramoto-Sivashinsky equation and the ADAPT forecasting model are detailed in section 6. We conclude with a discussion of hopeful applications of the MrEnKF as well as future improvements.

## 2 Wavelet Decomposition

Wavelet analysis has been used in a wide spectrum of applications where fidelity of information varies by location and frequency simultaneously or where one seeks to isolate a particular signal in both location and frequency. Wavelet analysis has its roots in Fourier analysis, where one decomposes a signal with respect to frequency. However, in Fourier analysis the frequency information is not localized in the original domain, which can be undesirable when performing time-series analysis or image processing. For this reason wavelet analysis, a localized frequency decomposition, was developed. The goal of this section is to establish notation that will be used throughout the paper and briefly revisit some concepts of wavelet decomposition. The wavelet analysis used in our work is based on the multiresolution decomposition of Mallat [48, 49]. For further details regarding wavelets we refer the reader to the work by Daubechies [16]

Suppose we are given a discretized signal  $f \in \mathbb{R}^n$ . We can perform an  $N$ -level wavelet transform [48] of the observed signal,  $w^f = \mathcal{W}_N f$  and group the coefficients by level,

$$w^f = \left[ (w_{N+1}^f)^T, (w_N^f)^T, (w_{N-1}^f)^T, \dots, (w_1^f)^T \right]^T.$$

Here  $w_{N+1}^f$  represents the coarsest coefficients and each successive  $w_i^f$ ,  $i = N, N - 1, \dots, 1$ ,

represents increasingly fine scale coefficients. We define the projections of the wavelet coefficients onto each scale by

$$P_i w^f = w_i^f, \quad i = N + 1, N, N - 1, \dots, 1. \quad (2.1)$$

In general the coarser wavelet coefficients capture larger scale behavior of the signal, each successive wavelet level captures finer scale variations [16, 48, 49].

For purposes of separating scales within the ensemble Kalman filter, it is necessary to compute the effect of the multi-scale decomposition on the covariance of both the model and the observation. If we assume that a signal has a Gaussian distribution,  $f \sim N(\mu_f, C_f)$ , then the wavelet coefficients are Gaussian distributed as well,  $w_i^f \sim N(\mu_i^f, C_i^f)$  for  $i = N + 1, \dots, 1$ . The mean and covariance for each level of wavelet coefficients is given by

$$\mu_i^f = P_i \mathcal{W}_N \mu_f, \quad C_i^f = P_i \mathcal{W}_N C_f (P_i \mathcal{W}_N)^T.$$

This result relies only on the linearity of the wavelet transform and projections. Here we have given formulas only for the covariance matrices for each level of the  $N$ -level wavelet transform, ignoring covariance terms between levels of the transform. It is worth noting that our proposed MrEnKF allows some interaction between scales though these interactions are not treated explicitly.

### 3 Multiresolution ENKF

Using the MRA decomposition introduced in the previous section we put forward a method of including scale dependent model and observation error information in the EnKF assimilation scheme. The method we propose is iterative, over scales, which allows for a limited increase in computational complexity over the standard EnKF methods. Moreover, the method we use to include the wavelet decomposition modifies the observation operator of the assimilation problem and therefore is agnostic toward the exact EnKF implementation, e.g. stochastic, square root, transform etc.

The common setup for the EnKF is as follows [15, 25, 40], an observation of a dynamical system is made with assumed Gaussian observational error,  $y_{\text{obs}} \sim N(\mu_{\text{obs}}, R)$ . The forecast (background) state, denoted  $x_b$ , is assumed to be generated by a mathematical model of the system. Due to model error the forecast state is assumed to be Gaussian distributed,  $x_b \sim N(\mu_b, C_b)$ . The forecast state is related to the observation through a, possibly nonlinear, observation operator  $H(\cdot)$  and we write the forecast observation as  $H(x_b)$ . The model is assumed to be unbiased so that  $\mu_{\text{obs}} = \mathbb{E}[H(x_b)]$ . Under these assumptions the pair  $(x_b, y_{\text{obs}})$  is jointly Gaussian distributed,

$$\begin{bmatrix} x_b \\ y_{\text{obs}} \end{bmatrix} \sim N \left( \begin{bmatrix} \mu_b \\ \mathbb{E}[H(x_b)] \end{bmatrix}, \begin{bmatrix} C_b & \text{Cov}(x_b, H(x_b)) \\ \text{Cov}(H(x_b), x_b) & \text{Cov}(H(x_b)) + R \end{bmatrix} \right). \quad (3.1)$$

We refer to the forecast state conditioned on the observations as the *analysis* state,  $x_a = x_b | y_{\text{obs}}$ . Given the preceding assumptions the analysis has Gaussian distribution and we write  $x_a \sim N(\mu_a, C_a)$  with

$$\begin{aligned} \mu_a &= \mu_b + \text{Cov}(x_b, H(x_b)) (\text{Cov}(H(x_b)) + R)^{-1} (y_{\text{obs}} - \mathbb{E}[H(x_b)]) \\ C_a &= C_b - \text{Cov}(x_b, H(x_b)) (\text{Cov}(H(x_b)) + R)^{-1} \text{Cov}(H(x_b), x_b). \end{aligned} \quad (3.2)$$

The analysis state of the system represents the distribution of likely system states given our most recent observations. In order to approximate draws of  $x_a$  the EnKF first generates a forecast *ensemble* of states  $x_b^\alpha$  for  $\alpha = 1, 2, \dots, M$ , where  $M$  is the size of the ensemble. The forecast ensemble is used to compute sample expectations and covariances to replace the terms  $\mu_b$ ,  $C_b$ ,  $\mathbb{E}[H(x_b)]$ ,  $\text{Cov}(x_b, H(x_b))$ , and  $\text{Cov}(H(x_b))$  in (3.2). Once (3.2) has been approximated using the forecast ensemble there are a myriad of methods to generate an analysis ensemble  $x_a^\alpha$ ,  $\alpha = 1, 2, \dots, M$ , approximating draws from  $N(\mu_a, C_a)$ . These methods include stochastic EnKF variations [24, 26], ensemble transform Kalman Filters (ETKF) [36], ensemble adjustment Kalman Filters [1], and ensemble square root Kalman filters [60, 62]. We refer to all of these methods loosely as ensemble Kalman filters. In our applications we use an ensemble transform Kalman filter [36]. Once the analysis ensemble is generated a new forecast is computed by propagating the analysis ensemble through the mathematical model until the next observation time and the whole process is iterated.

In order to include multi-scale information into the EnKF, we apply the wavelet decomposition to the observation operator  $H(\cdot)$ . In practice this means that the wavelet transform is applied to the data and ensemble of state observations as a preprocessing step. Decomposing  $H(\cdot)$  yields observed wavelet coefficients  $w_{\text{obs}} = \mathcal{W}_N y_{\text{obs}}$  and the unbiased observation assumption implies  $w_{\text{obs}} = \mathbb{E}[\mathcal{W}_N H(x_b)]$ . Scales are separated by applying the wavelet projections (2.1), yielding  $N + 1$  sets of scale dependent observations,

$$y_{\text{obs}}^i = P_i w_{\text{obs}}, \quad i = N + 1, N, \dots, 1 \quad (3.3)$$

with observation errors distributed as

$$y_{\text{obs}}^i \sim N(P_i \mathcal{W}_N \mu_{\text{obs}}, P_i \mathcal{W}_N R(P_i \mathcal{W}_N)^T). \quad (3.4)$$

For convenience we define the scale dependent observation operator as

$$H_i(x_b) = P_i \mathcal{W}_N H(x_b), \quad i = N + 1, N, \dots, 1 \quad (3.5)$$

and note that since the model is assumed unbiased

$$\mathbb{E}[y_{\text{obs}}^i] = \mathbb{E}[H_i(x_b)], \quad i = N + 1, N, \dots, 1. \quad (3.6)$$

With the above notation we may express the unbiased assumption at each scale as

$$y_{\text{obs}}^i = H_i(x_b) + \epsilon_i, \quad \epsilon_i \sim N(0, R_i) \quad (3.7)$$

where  $R_i = P_i \mathcal{W}_N R(P_i \mathcal{W}_N)^T$  for  $i = N + 1, N, \dots, 1$ .

Instead of conditioning  $x_b$  on all observation scales simultaneously we iteratively condition the forecast on the observations from one scale at a time. Largest scales are assimilated first followed by the assimilation of finer scales in the observations. Of course any other ordering is possible and perhaps the most accurately observed scales should be assimilated first.

We use the notation  $x_{N+2} = x_b$ ,  $\mu_{N+2} = \mu_b$ , and  $C_{N+2} = C_b$ . Our iterative multiresolution EnKF (MrEnKF) is then defined by the series of conditioned model states

$x_i = x_{i+1}|y_{\text{obs}}^i \sim N(\mu_i, C_i)$  for  $i = N + 1, N, \dots, 1$  with mean and covariance at each scale given by

$$\begin{aligned}\mu_i &= \mu_{i+1} + \text{Cov}(x_{i+1}, H_i(x_{i+1}))[\text{Cov}(H_i(x_{i+1})) + R_i]^{-1}(y_{\text{obs}}^i - \mathbb{E}[H_i(x_{i+1})]) \\ C_i &= C_{i+1} - \text{Cov}(x_{i+1}, H_i(x_{i+1}))[\text{Cov}(H_i(x_{i+1})) + R_i]^{-1}\text{Cov}(H_i(x_{i+1}), x_{i+1}).\end{aligned}\tag{3.8}$$

The final analysis, with all scales assimilated, then is distributed as  $x_a = x_1 = x_2|y_{\text{obs}}^1 \sim N(\mu_1, C_1)$ .

In practice each of the Gaussian distributions is approximated by an ensemble of model states. Any standard EnKF type algorithm can be used to form an analysis ensemble approximating a draw from the Gaussian conditioned by each successive scale. In our examples we have used the ensemble transform Kalman filter (ETKF) [36] to form the intermediate analysis ensembles but any EnKF variation could be applied. It is important to note two properties of our MrEnKF. First, we have made the important assumption that the *conditioning on the larger scale does not effect the bias at the finer scale*. Second, because the conditioning on scales is performed iteratively we did not need to make any assumptions about independence of scales and scale/scale covariance information is allowed to propagate through to the analysis.

## 4 Observation Covariance

For large problems the observation covariance transformation may be very expensive to compute at each level. Computing  $R_i = P_i \mathcal{W}_N R (P_i \mathcal{W}_N)^T$  for  $i = N + 1, N, \dots, 1$  requires calculating a wavelet transform for each dimension of the model forecast  $x_b$ . In cases where the data being assimilated is the discretization of a two or three dimensional field computing and storing this covariance matrix is computationally prohibitive. This is further complicated by the fact that the wavelet transform is not usually stored as a matrix, so computing  $(P_i \mathcal{W}_N)^T$  is not straight forward. Some of these problems can be simplified if we know the symmetric square root decomposition of the covariance matrix,  $R = SS^T$ . If the square root is available then at least the question of transposing the wavelet transform is averted and  $R_i = (P_i \mathcal{W}_N S)(P_i \mathcal{W}_N S)^T$ .

If the original covariance  $R$  is diagonal or very dominated by the diagonal terms we may be safe in making the assumption that  $R_i$  is a diagonal matrix with a constant on the diagonal determined by some overall measure of the noise level in the observations at each scale. This can be accomplished by setting

$$R_i = \lambda_i \sigma_{\max}^2(R), \quad i = N + 1, N, \dots, 1.\tag{4.1}$$

Here  $\sigma_{\max}(R)$  is the largest singular value of  $R$  and  $0 < \lambda_i$  is a scaling parameter to adjust the confidence given to observations at each scale. The latter approach has worked well in our examples (Section 6) but requires tuning of the scaling parameter and represents a drastic assumption about the observation error within each scale.

A more rigorous way of approximating the covariance for each observation scale relies on the sampling of observations and approximating the covariance at differing scales in

the spirit of the original EnKF proposed by Evensen [24, 26]. This method is accurate if one is willing to sample the observational noise determined by  $R$ . The method starts by generating  $M$  samples of  $\epsilon \sim N(0, R)$ ,  $\epsilon_j, j = 1, 2, \dots, M$ . To approximate  $R_i$  for a given wavelet scale each  $\epsilon_j$  is transformed to give  $\epsilon_j^i = P_i \mathcal{W}_N \epsilon_j$ . The transformed noise samples are then used to form a noise ensemble matrix

$$E_i = [\epsilon_1^i | \epsilon_2^i | \dots | \epsilon_M^i]. \quad (4.2)$$

The covariance is then approximated by

$$R_i \approx \frac{1}{M-1} E_i E_i^T. \quad (4.3)$$

The disadvantage of this approach is that we may require a large number of noise samples to accurately approximate  $R_i$ . However, if covariance inflation is to be used at each scale, a very accurate approximation may not be necessary. Moreover, at least the larger scale components will have a significantly lower dimension than the original forecast, and therefore will allow an accurately approximated covariance with far fewer samples than would be necessary to approximate the full covariance.

## 5 Ensemble Inflation

Ensemble inflation has been shown to be beneficial in preventing ensemble collapse and divergence when using ensemble data assimilation schemes [34, 61]. Moreover, in [43] it was shown that in order to have both stability and accuracy in an EnKF scheme inflation was necessary. The MrEnKF proposed makes it straightforward to apply a scale dependent inflation, making for a very robust/tunable filter. The analysis mean and covariance at each scale given in equation (3.8) can be replaced with

$$\begin{aligned} \mu_i &= \mu_{i+1} + \text{Cov}(x_{i+1}, H_i(x_{i+1})) \left[ \text{Cov}(H_i(x_{i+1})) + \frac{1}{\rho_i} R_i \right]^{-1} (y_{\text{obs}}^i - \mathbb{E}[H_i(x_{i+1})]) \\ C_i &= C_{i+1} - \text{Cov}(x_{i+1}, H_i(x_{i+1})) \left[ \frac{1}{\rho_i} \text{Cov}(H_i(x_{i+1})) + \frac{1}{\rho_i^2} R_i \right]^{-1} \text{Cov}(H_i(x_{i+1}), x_{i+1}) \end{aligned} \quad (5.1)$$

for  $i = N+1, N, \dots, 1$ . This implies that a vector of scale dependent inflation coefficients must be chosen,

$$\rho = (\rho_{N+1}, \rho_N, \dots, \rho_1)^T. \quad (5.2)$$

At each scale the coefficient  $0 < \rho_i$  quantifies the amount of confidence given to either the model or the observation during assimilation.

A scale dependent inflation allows the user to control the confidence in the model or observation at each scale separately. Therefore, if a set of observations is known to be a very accurate measure of one scale the inflation coefficient for this scale can be increased while the others are left unchanged. Allowing this level of tuning can be advantageous if there is detailed information available about the scale dependence of observation and model errors.

## 6 Example Applications

We give two examples where the use of an MrEnKF scheme is beneficial. Scale dependence can become important if the observation error varies greatly with scale or if the model error varies greatly with scale. In our first example we apply the MrEnKF to a chaotic nonlinear PDE in one dimension under the assumption of scale dependent observational noise. The second example demonstrates the MrEnKF on a problem in solar weather forecasting in which the model itself has scale dependent error. In both cases we demonstrate that separation of scales during the assimilation can significantly improve the ensemble's ability to track the observed data while reliably representing the error in the forecast.

### 6.1 Kuramoto-Sivashinsky Equation

The Kuramoto-Sivashinsky equation was named for its derivation in modeling hydrodynamic stability of laminar flame fronts [56] and as a phase equation for the complex Ginzburg-Landau equation [45]. It was first derived as a model of nonlinear saturation of drift waves associated with the oscillation of plasma particles trapped in magnetic wells [46]. Applications of the K-S equation include modeling of the dynamics of self-focusing lasers [51], instabilities in thin films [8], and the flow of a viscous fluid down a vertical plane [57]. Extensive numerical investigations of the chaotic dynamics of the K-S equation have been carried out [20, 37, 38, 44, 58]. Furthermore, the K-S equation has been a source of many results related to dynamics of chaotic systems [14, 23, 53]. In regards to assimilation and control the K-S equation has classically represented a challenging problem to test methods of control and assimilation for chaotic dynamical systems [18, 21, 22, 35, 39]. For an overview of the theory of existence and uniqueness of the K-S equation the interested reader is pointed to [55, 59].

In its simplest form the Kuramoto-Sivashinsky equation in one dimension is expressed as

$$\begin{aligned} u_t + u_{xx} + u_{xxxx} + uu_x &= 0 \quad \text{on } [-\pi L, \pi L] \times [0, T] \\ u(x, 0) = u_0(x), u(-\pi L, t) = u(\pi L, t) &\quad \text{for } t \geq 0, \end{aligned} \tag{6.1}$$

where  $L$  is a bifurcation parameter which controls the behavior of solutions, i.e. stable, periodic, chaotic, etc. Equation (6.1) is diagonalized by the Fourier transform to get the system of ODEs

$$\begin{aligned} u(x, t) &= \sum_n u_n(t) \exp\left(\frac{inx}{L}\right), \quad u_0(x) = \sum_n u_n(0) \exp\left(\frac{inx}{L}\right) \\ \frac{du_n}{dt} &= \left(\frac{n}{L}\right)^2 \left(1 - \left(\frac{n}{L}\right)^2\right) u_n - \frac{in}{2L} \sum_{j \in \mathbb{Z}} u_j(t) u_{n-j}(t). \end{aligned} \tag{6.2}$$

This diagonalization shows that the first  $0 \leq n < L$  Fourier modes are unstable about  $u_n(t) = 0$  while the higher Fourier modes are stable [42, 55, 59]. The nonlinear term then allows mixing between the low and high Fourier modes which allows for stable solutions as some of the energy is transferred from the low to the high modes and then dissipated [55, 59]. This property of the K-S equation makes it ideal for testing a scale dependent



EnKF since we can assume that the unstable low frequencies, large scales, are observed with higher accuracy than the high frequencies, small scales, and investigate the effect of propagating scale dependent information through the EnKF.

In our data assimilation experiments with the K–S equation we assume  $L = 22$  which is well into the regime of chaotic solutions [39, 42]. Our experiment’s initial condition’s are chosen as in the work of [39, 42],

$$u_0(x) = \cos\left(\frac{x}{L}\right) \left(1 + \sin\left(\frac{x}{L}\right)\right). \quad (6.3)$$

Solutions to the K–S equation are simulated using a stable fourth order Runge-Kutta scheme with exponential time differencing [39, 42]. The spatial domain is discretized using 512 equally spaced points on  $-\pi L < x_j \leq \pi L$ , the temporal domain is discretized using a step length of  $\Delta t = 0.5$ . We assume that solutions of (6.1) are observed, until time  $T = 300$ , every  $20^{\text{th}}$  time-step  $t_n = 20n\Delta t$ . Observations of the K–S solution will be denoted by  $H(u(t_n)) = (u(x_1, t_n), u(x_2, t_n), \dots, u(x_{512}, t_n))^T$ .

We set up a *twin* experiment with the K–S equation to compare the performance of the EnKF and MrEnKF. The twin experiment consists of simulating observations from a reference solution of the K–S equation having initial conditions given by (6.3). Observations are generated from this reference solution at each of the time points  $t_n$  and Gaussian noise, as specified in the next paragraph, is added to the observations. For both the EnKF and MrEnKF ensembles are initialized by adding Gaussian white noise with standard deviation  $\sigma = 0.8$  to the initial condition (6.3). The ensemble size in all experiments was taken to be  $N = 50$ . The ensemble members are propagated forward according to the K–S equation to time  $t_1$  and assimilation is performed using the synthetic observations. This is repeated at each  $t_n$  and the results of the assimilation are compared.

Scale dependent observation error is modeled by taking a level-4 wavelet transform of the solution at each  $t_n$  using a Daubechies ‘db9’ wavelet with 9 vanishing moments [16]. Gaussian white noise is then added to each level of wavelet coefficients with standard deviation dependent on the transform level of the coefficients. The standard deviation of the additive noise at each wavelet level was chosen so that the signal-to-noise ratio (SNR) was smaller for the fine scale coefficients, thus keeping more of the large scale information in the observations. Specifically, the standard deviations for the Gaussian noise added to the four levels of wavelet coefficients were taken to be  $\sigma_5 = 0.75$ ,  $\sigma_4 = 0.75$ ,  $\sigma_3 = 1.65$ ,  $\sigma_2 = 1.0$ ,  $\sigma_1 = 0.0008$ . This choice of standard deviation gave an average SNR of  $\text{SNR}_5 \approx 18.22$ ,  $\text{SNR}_4 \approx 15.58$ ,  $\text{SNR}_3 \approx 2.04$ ,  $\text{SNR}_2 \approx 1.16$ , and  $\text{SNR}_1 \approx 1.17$  at the respective scales. Average SNR values were calculated by applying the formula

$$\text{SNR}_i = \frac{\max(w_i) - \min(w_i)}{\sigma_{\text{noise}}}, \quad i = N + 1, N, \dots, 1 \quad (6.4)$$

to each scale of the wavelet coefficients and then averaging each scale’s SNR over all observation times. Here  $\max(w_i)$  is the maximum wavelet coefficient at level  $i$ , similarly  $\min(w_i)$  is the minimum wavelet coefficient at level  $i$ . The actual deviations of the simulated observations, with this noise structure, from the true solution were Gaussian and had a standard deviation of  $\sigma_{\text{obs}} = 0.8$ .

The EnKF and the MrEnKF were applied to the Kuramoto-Sivashinsky assimilation problem with scale independent noise. In this case the EnKF and the MrEnKF both resulted in ensembles that tracked the solution very well for Gaussian observation noise with a standard deviation of  $\sigma_{\text{obs}} = 0.8$ . The EnKF and MrEnKF were then compared using the scale dependent observation noise structure described above. To visualize the ensemble’s ability to track the true solution of the K–S equation we present the ensemble tracking at three distinct points within the domain  $[-\pi L, \pi L]$ . Figure 1 shows the true solution of the

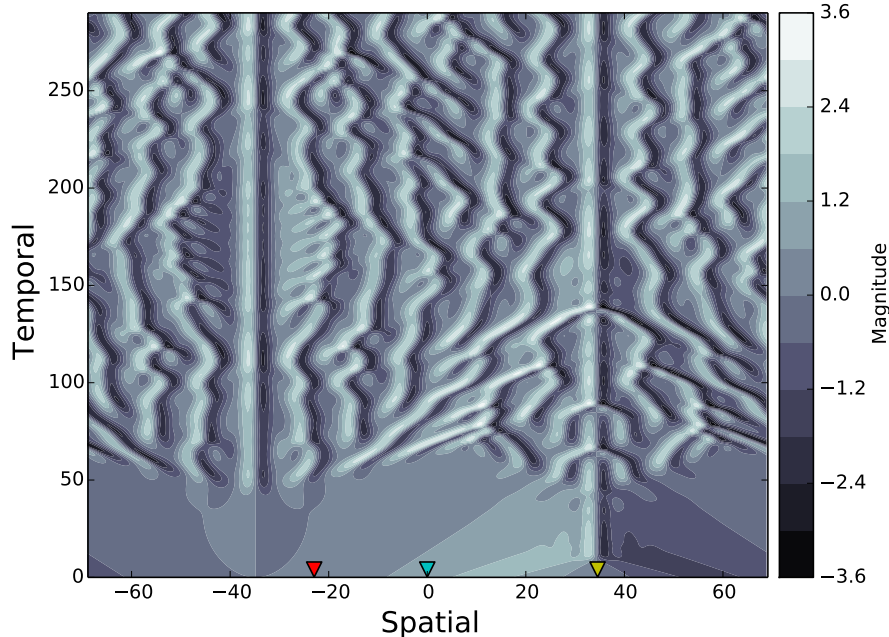


Figure 1: Our reference solution for the K–S equation is shown as a contour plot. The red, cyan, and yellow markers indicate points where our ensemble forecasts are presented in Figure 2. Observations were generated by adding scale dependent Gaussian noise to this solution.

K–S equation used to generate observations along with three markers indicating the spatial points where ensemble tracking is illustrated in Figure 2. The K–S solution with initial condition (6.3) has two stationary nodes at  $x = \pm \frac{L\pi}{2}$ . We illustrate the ensemble tracking near the first stationary node  $\hat{x}_1 = -7.3\pi$ , away from both stationary nodes  $\hat{x}_2 = 0.0$ , and on the second stationary node  $\hat{x}_3 = 11.0\pi$ . At  $\hat{x}_3$  both the EnKF and the MrEnKF have difficulties tracking the solution. This is due to the fact that locally the K–S solution is not stationary and therefore the incorporation of this local information in the EnKF and the MrEnKF tends to pull the ensemble away from zero. However, the MrEnKF still envelops the stationary solution much better, though with an admittedly high ensemble standard deviation. At the points  $\hat{x}_1$  and  $\hat{x}_2$  the EnKF reduces the ensemble spread very quickly and then can be forced off of the true solution randomly (left plots in Figure 2). The MrEnKF does not have this behavior (right plots in Figure 2), though it must pay the cost of maintaining a larger ensemble spread. The MrEnKF ensemble almost always envelops the true solution and therefore offers a significant advantage. The advantages of the MrEnKF become clearer if we compare the rank histograms [29] for the EnKF and MrEnKF.

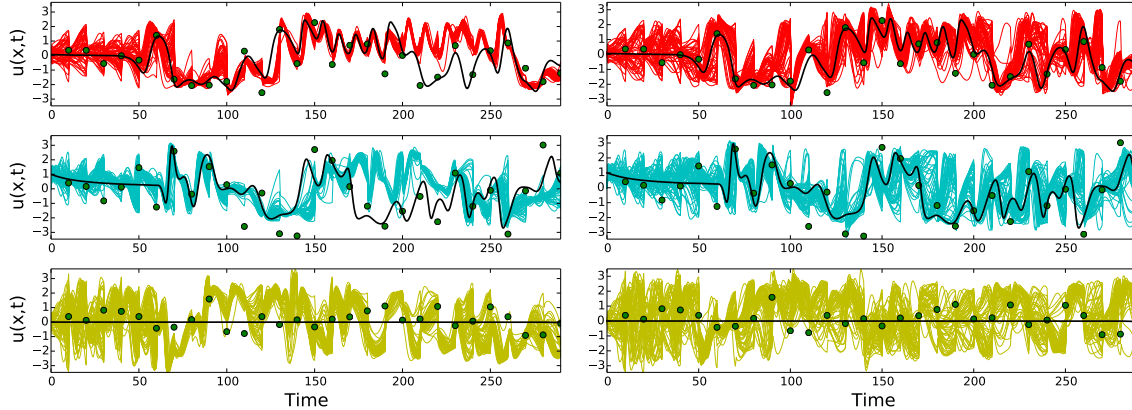


Figure 2: Tracking of a solution of the K–S equation using the EnKF (LEFT) and MrEnKF (RIGHT). Ensemble colors correspond to the marker colors in Figure 1. The true solution values at each point are shown in black while the solution observations are shown with green dots. Scale dependent noise has been added to the observations of this solution as described. We see that the ensemble, under EnKF, has significant periods of divergence from the true solution. More problematic is the fact that the standard deviation of the ensemble is small compared to the observational noise indicating a great deal of confidence in the assimilation. The MrEnKF on the other hand is shown to track the solution in the sense that usually the ensemble envelops the true solution. The standard deviation of the ensemble is kept large by taking into account scale dependent observation error. Due to the large ensemble spread the  $L^2$  discrepancy, Figure 4, for the MrEnKF is only incrementally better than for the EnKF. However, the standard deviation is more in line with the true observation error and the forecast spread reflects the variance in the true solution more accurately as demonstrated by the rank histograms in Figure 3

The EnKF rank histogram has a very U-shaped distribution indicating that the true solution is most often found in the tails of the forecast distribution (left plot in Figure 3). On the other hand, the MrEnKF rank histogram is close to uniform (right plot in Figure 3) indicating that the forecast ensemble spread is a reliable representation of the true variation in the solution given by the observed data. For a secondary measure of performance evaluation we compute the  $L^2$ -norm of the difference between the reference solution and the assimilation ensemble mean, which we will refer to as the  $L^2$ -discrepancy for the mean. In this measure, we again see that the MrEnKF outperforms the standard EnKF (Figure 4). The majority of the time, the MrEnKF discrepancy is smaller than the EnKF discrepancy, which indicates that MrEnKF provides a more accurate forecast. Both methods exhibit oscillations in the  $L^2$ -discrepancy, where we see a sudden decrease in discrepancy where we perform assimilation, and then a significant increase, indicating that the model is deviating from the true solution. The deviation is due to the chaotic dynamics within the K–S equation, which is reflected in the tendency of the ensemble to spread out and away from the analysis after some time.

## 6.2 Solar Photosphere

We apply the MrEnKF to a problem in solar weather using the Air Force Data Assimilative Photospheric Flux Transport Model (ADAPT) [5, 6, 7, 33]. In ADAPT the magnetic flux

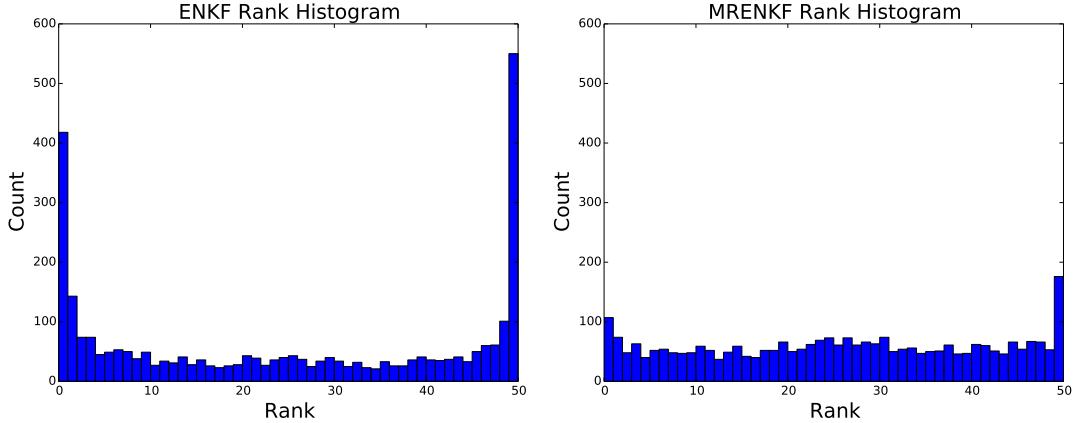


Figure 3: Rank histograms are presented for the K-S assimilation investigation using the EnKF (left) and MrEnKF (right). These were generated by ranking the ensemble forecasts at 50 equally spaced spatial points every  $10^{th}$  time step, in order to reduce the effects of spatio-temporal correlations, and observing the rank that the true solution occurred in. For both the EnKF and MrEnKF these ranks were binned and the above histograms were formed. If the ensemble spread accurately represents the distribution of where the true solution is expected to fall given the observations then the rank histogram should be approximately uniform. In the above images we see that the EnKF rank histogram is very U-shaped, indicating an ensemble forecast that has collapsed. The rank histogram for the MrEnKF is much more uniform and therefore indicates a more accurate representation of the true solution’s distribution given the observations.

is propagated across the Sun’s surface using the combined effects of differential rotation, meridional flow, and super granular diffusion [33, 64]. ADAPT does well at accurately transporting flux that is already present in the model ensemble’s forecast. However, solar physicists are interested in the tracking of emergent coherent regions of magnetic flux of the same sign. These large clumps of magnetic flux are known as *active regions* and are primary drivers of large space weather events such as Coronal Mass Ejections (CMEs) [4, 27, 28, 52]. The underlying dynamic ADAPT model has no mechanism in place to generate these active regions since the physics of their appearance is still not well understood. Therefore, the ADAPT simulation has significant model error at the scale of active regions.

ADAPT is updated using observations of the photospheric flux on the Earth side of the Sun with an expert informed model of observation error, see Figure 5. The model of observational noise used by solar physicists assumes uncorrelated, zero mean, Gaussian measurement noise at each pixel with a standard deviation that grows as the observation boundary is approached [31, 32]. Observation error is greater near the edges of the visible region of the Sun (right plot in Figure 5), since only the radial component of the magnetic flux is observed and the accuracy of this observation is proportional to how aligned the observatory is with the direction of the radial component at a point on the solar surface. Inevitably the edges of the visible portion of the photosphere have radial directions not aligned with Earth and thus the *limbs* of the observation region are associated with greater error [31, 32].

This model of measurement error does not have any scale dependence. However, strong fluctuations in the magnetic flux of the photosphere appear clumped together in large *active*

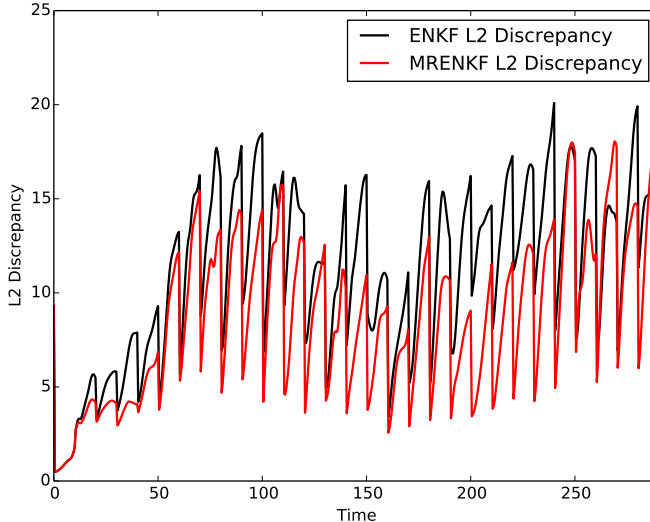


Figure 4: Here we show the  $L^2$  discrepancy between the true solution to the K-S equation and the mean of the ensemble forecast for the EnKF scheme (black) and MrEnKF scheme (red). We see that the MrEnKF scheme usually results in a lower forecast discrepancy. This fact coupled with the fact that the rank histogram is much more uniform for the MrEnKF, Figure 3, shows that the MrEnKF offers many advantages to the scale independent EnKF in this scenario. The discrepancy was calculated by computing the mean of the forecast at each time step and computing the  $L^2$  difference between the mean and the true solution at every time step.

*regions* [52]. When an active region is observed, i.e. a large coherent region of magnetic flux all of the same sign, solar physicists trust the observation and want to see that region represented in the ensemble. This is especially important if the active region is newly emerged into the observed region of the photosphere. Any data assimilative algorithm used for magnetic flux forecasting should therefore assign more trust to large coherent regions of magnetic flux with the same sign and thus insert the observed active region into the analysis ensemble. This can not be done by the standard EnKF with uncorrelated pixel-by-pixel Gaussian measurement noise since the scale of an observed feature does not effect its confidence during assimilation. A scale dependent ensemble Kalman filter can make progress toward resolving this data assimilation problem.

Unlike our previous example with the Kuramoto-Sivashinsky equation, in which scale dependent observation noise necessitated the use of the MrEnKF, our solar weather example has scale dependent *model error*. In the ADAPT model of photospheric flux dynamics there is no mechanism for the creation of new active regions since these are caused by physical processes occurring below the observable surface of the Sun. From the perspective of the solar observation instruments the pixel-by-pixel representation of observation error is sensible. However, since the model has no way to insert large scale active regions, and these can arise over a short time span relative to the cadence of solar observations, the model will necessarily be diverged from observations of active regions that have appeared since the last observation. This effect is especially apparent when active regions appear on the *east limb* (left side, Figure 5) of the observation region since these solar regions have just emerged from the far side of the Sun and have not been observed for a long span of time.

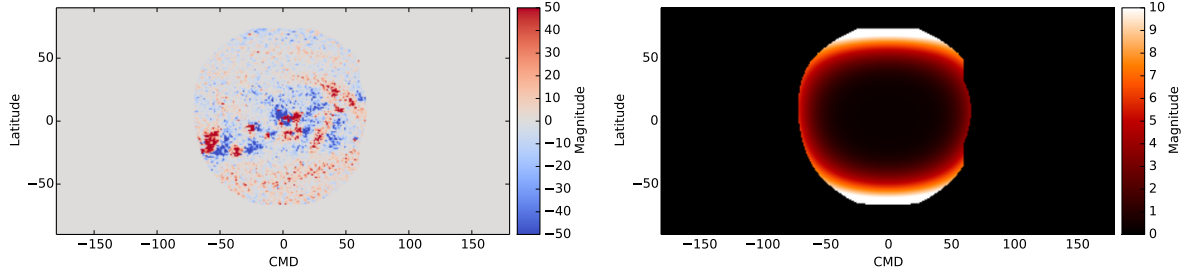


Figure 5: (LEFT) An example observation from the SOLIS vector spectro-magnetograph (VSM). The SOLIS-VSM provides observations of the radial magnetic flux from between  $\pm 60^\circ$  latitude and  $\pm 90^\circ$  longitude, centered on the central meridian. The cadence of these observations is roughly one image every 24 hours. These observations are then assimilated into ADAPT’s evolving global map of the photospheric magnetic flux. Active regions are pictured as large coherent areas of magnetic flux with the same sign and are primary drivers of large scale solar weather events. As the sun rotates these active regions emerge on the *east limb* (left side of the observation region) and then continue to be transported across the observation region. Since the radial magnetic flux is observed the curvature of the Sun near the boundaries of the observation region causes a larger observation error near the east limb. However, observations of active regions emerging on the east limb are trusted by solar weather experts and therefore should be assigned a high confidence during assimilation. (RIGHT) Pixel-by-pixel standard deviation associated with the SOLIS-VSM observation region (a standard deviation of 0 corresponds to unobserved regions of the solar surface). The standard deviation in the center of the observation region are small but non-zero. Near the boundaries of the observation region the radial magnetic field has much higher observation error due to the curvature of the Sun’s surface. This causes traditional EnKF methods to discard observations on the boundaries of the observation region. However, active regions near the boundaries are trusted a great deal by solar physicists and thus the MrEnKF serves an important purpose in assigning more trust to the observation of these large scale features.

The implication is that the MrEnKF can serve a useful purpose in preparing solar weather forecasts by systematically assigning a high confidence to observed structures at large scales and a low confidence to observed structures occurring at small scales within the ADAPT ensemble. This weighting is accomplished by reducing the assumed observation error and increasing the ensemble inflation factor at large scales.

Unlike our K-S example the ADAPT model state and observations exist in  $\mathbb{R}^2$  and therefore a two dimensional wavelet must be used. There exist several ways to generalize one dimensional wavelets to higher dimensions, in this work we use the tensor products [16, 48, 49] of Daubechies ’db9’ wavelets and only use a two level transformation on the SOLIS-VSM observations. Figures 6 and 7 compare the effect of using the EnKF and MrEnKF to assimilate an active region emerging on the east limb of the solar photosphere. The active region tracked in Figures 6 and 7 emerged into the SOLIS-VSM observation region on November 18<sup>th</sup> 2003 at 18:35. Observation and assimilation of this active region is shown as it passes across the observation region and then exits on the West limb. We can see that the EnKF has difficulties retaining scale dependent coherent features of the active region in Figure 6. The diffusion of the active region in the EnKF algorithm becomes more pronounced as the active region is tracked across the solar surface. As the active region exits the observation region and crosses to the far side of the Sun the ensemble has almost completely diverged from observations in the neighborhood of the active region. When we examine the MrEnKF assimilation of the active region in Figure 7 we see that the

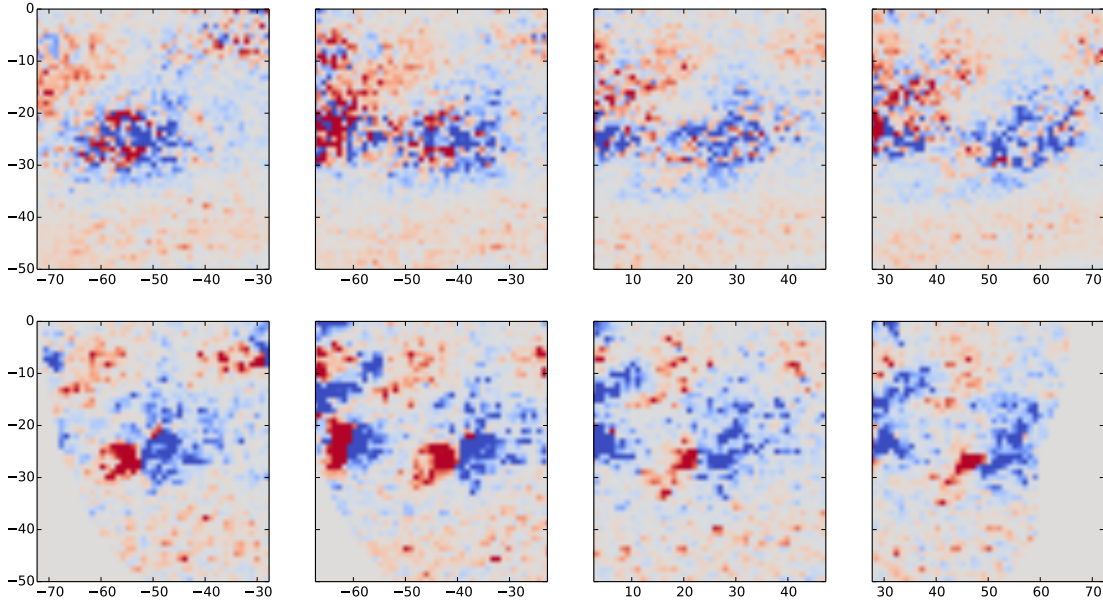


Figure 6: Here we illustrate the effect of using a scale independent EnKF assimilation scheme on a small active region. The top row corresponds to the mean of the EnKF forecast while the bottom row corresponds to the SOLIS-VSM observations. Red and blue regions represent positive and negative polarity regions respectively, the active region in question appears as a horizontal red and blue pair centered in each frame of the observations. The  $x$  and  $y$  axis of each frame represent the location on the solar surface in latitude-longitude using *Central Meridian Distance* (CMD) for the longitudinal coordinates. Observation times, from left to right, are the 18<sup>th</sup> of November 2003 at 18:35, the 19<sup>th</sup> of November 2003 at 18:11, the 24<sup>th</sup> of November 2003 at 17:05, and the 26<sup>th</sup> of November 2003 at 17:49. We can see that the EnKF disperses the active region when it first appears on the East limb. This dissipation of the active region then continues as the active region is tracked across the observation region until the active region is almost completely dissipated in the forecast before it exits the observation region. This error greatly reduces the utility of the EnKF solar forecast.

method preserves a more coherent structure of the active region. Moreover, as the active region is tracked across the observation region it becomes more resolved. This is due to the MrEnKF's ability to assign greater confidence to observed features at the scale of active regions. Since, once the active region exits on the West limb, it will not be observed again until it traverses the far side of the Sun it is paramount to have a good estimation of the size and intensity of the active region before it exits the observation region.

## 7 Discussion

We have detailed a method for inserting scale dependent information into an ensemble Kalman filter framework. Our method was demonstrated on a 1D nonlinear partial differential equation with scale dependent observation noise and on an example from solar weather forecasting in which the model error, due to missing physics, was highly scale dependent. The MrEnKF has the ability to account for scale dependent variations in observation and model accuracy and therefore tracked the evolving true solution of the

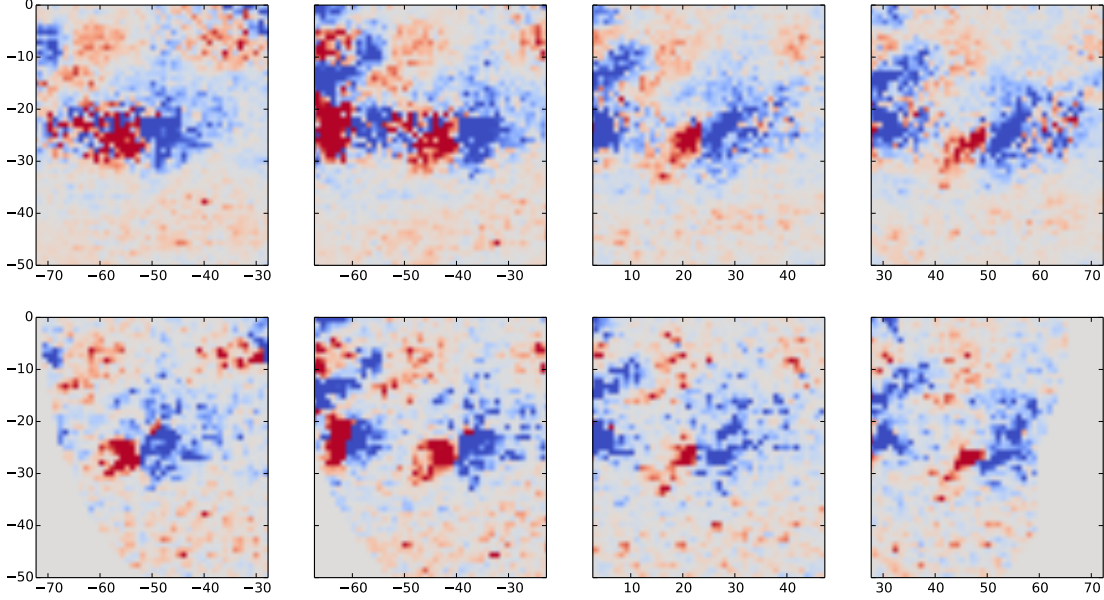


Figure 7: Here we illustrate the effect of using our MrEnKF assimilation scheme on a small active region. The top row corresponds to the mean of the MrEnKF forecast while the bottom row corresponds to the SOLIS-VSM observations. Red and blue regions represent positive and negative polarity regions respectively, the active region in question appears as a horizontal red and blue pair centered in each frame of the observations. The  $x$  and  $y$  axis of each frame represent the location on the solar surface in latitude-longitude using *Central Meridian Distance* (CMD) for the longitudinal coordinates. Observation times, from left to right, are the 18<sup>th</sup> of November 2003 at 18:35, the 19<sup>th</sup> of November 2003 at 18:11, the 24<sup>th</sup> of November 2003 at 17:05, and the 26<sup>th</sup> of November 2003 at 17:49. We can see that the MrEnKF preserves the coherent structure of the active region since more confidence has been assigned to observations occurring at the scale of active regions. As the active region is then repeatedly observed during its journey across the observation region the MrEnKF refines the forecast structure of the region. Notice that the active region forecast is still well resolved as it exits the observation region on the West limb.

Kuramoto–Sivashinsky equation more accurately than the standard EnKF for small ensemble size. The MrEnKF was also able to allow for scale dependent model deviations from observations in our solar photosphere example.

The effect of scale dependent observations and model errors are common in many scientific applications where forecasting is of interest. This problem is usually handled in an *ad hoc* way in practice by utilizing expert opinions of the forecast’s accuracy and manually adjusting observation error accordingly on a point-by-point basis. By combining the EnKF with a multi-scale wavelet analysis we have provided a general method to insert scale dependent information, regarding model accuracy and observation accuracy, into the assimilation scheme. Potential applications abound in areas of atmospheric and oceanic forecasting in which models may be accurate for large scale, non-turbulent effects, but highly unreliable at smaller scales.

In the Kuramoto-Sivashinsky application we demonstrated that, when the observation error is scale dependent, and the ensemble size is small the MrEnKF can be tuned to track the ground truth with less bias and more accuracy than the EnKF. The rank histogram



of the MrEnKF exhibited a more uniform distribution than that of the EnKF, implying that the ensemble distribution for the MrEnKF more accurately represented the observation probability distribution. Multiresolution analysis combined with the EnKF was motivated, for the authors, by the photospheric forecasting problem in solar weather. To this end we have demonstrated the MrEnKF’s effectiveness at preserving coherent structures observed on the photosphere known as active regions. The EnKF has difficulty capturing active region features in the analysis ensemble since the underlying forecast model does not have physics to generate emerging active regions. We plan to pursue a detailed study of active region assimilation using the MrEnKF in forthcoming publications.

The MrEnKF method does need further development to be a readily *out-of-the-box* applicable tool. In particular the decision of which wavelet basis to use and what level of wavelet transform to apply will be explored in future work. In our applications several multiresolution levels and wavelet types were experimented with. We note that the results did not seem particularly sensitive to the choice of wavelet. Moreover, the level of wavelet transform should be mostly informed by expert knowledge of the scale at which observation accuracy shifts or model accuracy shifts. Currently we solve this problem experimentally but plan to investigate adaptive methods in future work.

Another research topic in fully developing the MrEnKF is to put forward a reliable method to choose the ensemble inflation parameter at each scale. In our examples we tuned the inflation at each scale through experimentation. This is feasible if the number of multiresolution levels is small but would become impractical for a high number of wavelet transform levels. The methods pursued in [2, 3, 47, 61, 63, 65] involving an adaptive covariance inflation could circumvent this difficulty. We intend to investigate these types of adaptive inflation schemes in the context of our multiresolution EnKF in the future.

## 8 Acknowledgments

This research was primarily supported by NASA Living With a Star project #NNA13AB92I, “Data Assimilation for the Integrated Global- Sun Model”. Additional support was provided by the Air Force Office of Scientific Research project R-3562-14-0, “Incorporation of Solar Far-Side Active Region Data within the Air Force Data Assimilative Photospheric Flux Transport (ADAPT) Model”. The photospheric observations used in Figures 5, 6, and 7 were provided by SOLIS-VSM.

## References

- [1] Jeffrey L Anderson. An ensemble adjustment kalman filter for data assimilation. *Monthly weather review*, 129(12):2884–2903, 2001.
- [2] Jeffrey L Anderson. An adaptive covariance inflation error correction algorithm for ensemble filters. *Tellus A*, 59(2):210–224, 2007.
- [3] Jeffrey L Anderson. Spatially and temporally varying adaptive covariance inflation for ensemble filters. *Tellus A*, 61(1):72–83, 2009.

- [4] SK Antiochos, CR DeVore, and JA Klimchuk. A model for solar coronal mass ejections. *The Astrophysical Journal*, 510(1):485, 1999.
- [5] C Nick Arge, Carl J Henney, Irene Gonzalez Hernandez, W Alex Toussaint, Josef Koller, and Humberto C Godinez. Modeling the corona and solar wind using ADAPT maps that include far-side observations. In *SOLAR WIND 13: Proceedings of the Thirteenth International Solar Wind Conference*, volume 1539, pages 11–14. AIP Publishing, 2013.
- [6] C Nick Arge, Carl J Henney, Josef Koller, C Rich Compeau, Shawn Young, David MacKenzie, Alex Fay, and John W Harvey. Air force data assimilative photospheric flux transport (ADAPT) model. Technical report, DTIC Document, 2010.
- [7] CN Arge, CJ Henney, J Koller, WA Toussaint, JW Harvey, and S Young. Improving data drivers for coronal and solar wind models. In *5th International Conference of Numerical Modeling of Space Plasma Flows (ASTRONUM 2010)*, volume 444, page 99, 2011.
- [8] AJ Babchin, AL Frenkel, BG Levich, and GI Sivashinsky. Nonlinear saturation of rayleigh–taylor instability in thin films. *Physics of Fluids (1958-1988)*, 26(11):3159–3161, 1983.
- [9] Jonathan D Beezley, Jan Mandel, and Loren Cobb. Wavelet ensemble kalman filters. *arXiv preprint arXiv:1102.5554*, 2011.
- [10] Mark Buehner. Evaluation of a spatial/spectral covariance localization approach for atmospheric data assimilation. *Monthly Weather Review*, 140(2):617–636, 2012.
- [11] Mark Buehner and Martin Charron. Spectral and spatial localization of background-error correlations for data assimilation. *Quarterly Journal of the Royal Meteorological Society*, 133(624):615–630, 2007.
- [12] B Casati, G Ross, and DB Stephenson. A new intensity-scale approach for the verification of spatial precipitation forecasts. *Meteorological Applications*, 11(02):141–154, 2004.
- [13] Kenneth C Chou, Stuart A Golden, and Alan S Willsky. Multiresolution stochastic models, data fusion, and wavelet transforms. *Signal Processing*, 34(3):257–282, 1993.
- [14] Pierre Collet, Jean-Pierre Eckmann, Henri Epstein, and Joachim Stubbe. A global attracting set for the kuramoto-sivashinsky equation. *Communications in mathematical physics*, 152(1):203–214, 1993.
- [15] R. Daley. *Atmospheric Data Analysis*. Cambridge University Press, 1991.
- [16] Ingrid Daubechies et al. *Ten lectures on wavelets*, volume 61. SIAM, 1992.
- [17] Alex Deckmyn and Loik Berre. A wavelet approach to representing background error covariances in a limited-area model. *Monthly weather review*, 133(5):1279–1294, 2005.

- [18] Michael Desertion, Nikolaos Kazantzis, et al. Improved performance of the controlled kuramoto-sivashinsky equation via actuator and controller switching. In *American Control Conference, 2004. Proceedings of the 2004*, volume 1, pages 267–272. IEEE, 2004.
- [19] Robert W Dijkerman and Ravi R Mazumdar. Wavelet representations of stochastic processes and multiresolution stochastic models. *Signal Processing, IEEE Transactions on*, 42(7):1640–1652, 1994.
- [20] Jason T Drotar, Y-P Zhao, T-M Lu, and G-C Wang. Numerical analysis of the noisy kuramoto-sivashinsky equation in  $2+1$  dimensions. *Physical Review E*, 59(1):177, 1999.
- [21] Stevan Dubljevic. Model predictive control of kuramoto–sivashinsky equation with state and input constraints. *Chemical Engineering Science*, 65(15):4388–4396, 2010.
- [22] NH El-Farra, MA Demetriou, and PD Christofides. Actuator and controller scheduling in nonlinear transport-reaction processes. *Chemical Engineering Science*, 63(13):3537–3550, 2008.
- [23] John N Elgin and Xuesong Wu. Stability of cellular states of the kuramoto-sivashinsky equation. *SIAM Journal on Applied Mathematics*, 56(6):1621–1638, 1996.
- [24] Geir Evensen. Sequential data assimilation with a nonlinear quasi-geostrophic model using monte carlo methods to forecast error statistics. 1994.
- [25] Geir Evensen. *Data assimilation: The ensemble Kalman filter*. Springer, 2009.
- [26] Geir Evensen and Peter Jan Van Leeuwen. Assimilation of geosat altimeter data for the agulhas current using the ensemble kalman filter with a quasigeostrophic model. *Monthly Weather Review*, 124(1):85–96, 1996.
- [27] DA Falconer, RL Moore, and GA Gary. Correlation of the coronal mass ejection productivity of solar active regions with measures of their global nonpotentiality from vector magnetograms: Baseline results. *The Astrophysical Journal*, 569(2):1016, 2002.
- [28] Alexi Glover, Neale DR Ranns, Louise K Harra, and J Leonard Culhane. The onset and association of cmes with sigmoidal active regions. *Geophysical research letters*, 27(14):2161–2164, 2000.
- [29] Thomas M Hamill. Interpretation of rank histograms for verifying ensemble forecasts. *Monthly Weather Review*, 129(3):550–560, 2001.
- [30] Daniel Harris, Efi Foufoula-Georgiou, Kelvin K Droegemeier, and Jason J Levit. Multiscale statistical properties of a high-resolution precipitation forecast. *Journal of Hydrometeorology*, 2(4):406–418, 2001.
- [31] CJ Henney, CU Keller, and JW Harvey. Solis-vsm solar vector magnetograms. *arXiv preprint astro-ph/0612584*, 2006.

- [32] CJ Henney, CU Keller, JW Harvey, MK Georgoulis, NL Hadder, AA Norton, N-E Raouafi, and RM Toussaint. Solis vector spectromagnetograph: status and science. *arXiv preprint arXiv:0801.0013*, 2007.
- [33] Kyle S Hickmann, Humberto C Godinez, Carl J Henney, and C Nick Arge. Data assimilation in the adapt photospheric flux transport model. *Solar Physics*, 290(4):1105–1118, 2015.
- [34] P.L. Houtekamer and H.L. Mitchell. Data assimilation using an ensemble Kalman filter technique. *Mon. Wea. Rev.*, 126:796–811, 1998.
- [35] Changbing Hu and Roger Temam. Robust boundary control for the kuramoto-sivashinsky equation. In *Optimal control and partial differential equation. Conference*, pages 353–362, 2001.
- [36] Brian R Hunt, Eric J Kostelich, and Istvan Szunyogh. Efficient data assimilation for spatiotemporal chaos: A local ensemble transform kalman filter. *Physica D: Nonlinear Phenomena*, 230(1):112–126, 2007.
- [37] James M Hyman and Basil Nicolaenko. The kuramoto-sivashinsky equation: a bridge between pde’s and dynamical systems. *Physica D: Nonlinear Phenomena*, 18(1):113–126, 1986.
- [38] James M Hyman, Basil Nicolaenko, and Stéphane Zaleski. Order and complexity in the kuramoto-sivashinsky model of weakly turbulent interfaces. *Physica D: Nonlinear Phenomena*, 23(1):265–292, 1986.
- [39] M Jardak, IM Navon, and M Zupanski. Comparison of sequential data assimilation methods for the kuramoto–sivashinsky equation. *International journal for numerical methods in fluids*, 62(4):374–402, 2010.
- [40] Eugenia Kalnay. *Atmospheric modeling, data assimilation, and predictability*. Cambridge University Press, 2003.
- [41] Ivan Kusanický, Jan Mandel, and Martin Vejmelka. Spectral diagonal ensemble kalman filters. *arXiv preprint arXiv:1501.00219*, 2014.
- [42] Aly-Khan Kassam and Lloyd N Trefethen. Fourth-order time-stepping for stiff pdes. *SIAM Journal on Scientific Computing*, 26(4):1214–1233, 2005.
- [43] DTB Kelly, KJH Law, and AM Stuart. Well-posedness and accuracy of the ensemble kalman filter in discrete and continuous time. *Nonlinearity*, 27(10):2579, 2014.
- [44] Farhad Khellat and Nastaran Vasegh. The kuramoto–sivashinsky equation revisited: Low-dimensional corresponding systems. *Communications in Nonlinear Science and Numerical Simulation*, 19(9):3011–3022, 2014.
- [45] Yoshiki Kuramoto and Toshio Tsuzuki. Persistent propagation of concentration waves in dissipative media far from thermal equilibrium. *Progress of theoretical physics*, 55(2):356–369, 1976.

- [46] Robert Eugene LaQuey, SM Mahajan, PH Rutherford, and WM Tang. Nonlinear saturation of the trapped-ion mode. *Physical Review Letters*, 34(7):391, 1975.
- [47] Hong Li, Eugenia Kalnay, and Takemasa Miyoshi. Simultaneous estimation of covariance inflation and observation errors within an ensemble kalman filter. *Quarterly Journal of the Royal Meteorological Society*, 135(639):523–533, 2009.
- [48] Stephane G Mallat. Multiresolution approximations and wavelet orthonormal bases of  $l^2(r)$ . *Transactions of the American Mathematical Society*, 315(1):69–87, 1989.
- [49] Stephane G Mallat. A theory for multiresolution signal decomposition: the wavelet representation. *Pattern Analysis and Machine Intelligence, IEEE Transactions on*, 11(7):674–693, 1989.
- [50] Elias Masry. Covariance and spectral properties of the wavelet transform and discrete wavelet coefficients of second-order random fields. *Signal processing*, 64(2):131–143, 1998.
- [51] M Münkkel and F Kaiser. An intermittency route to chaos via attractor merging in the laser-kuramoto-sivashinsky equation. *Physica D: Nonlinear Phenomena*, 98(1):156–170, 1996.
- [52] Andrés Muñoz-Jaramillo, Dibyendu Nandy, Petrus CH Martens, and Anthony R Yeates. A double-ring algorithm for modeling solar active regions: unifying kinematic dynamo models and surface flux-transport simulations. *The Astrophysical Journal Letters*, 720(1):L20, 2010.
- [53] Basil Nicolaenko, Bruno Scheurer, and Roger Temam. Some global dynamical properties of the kuramoto-sivashinsky equations: Nonlinear stability and attractors. *Physica D: Nonlinear Phenomena*, 16(2):155–183, 1985.
- [54] Tim N Palmer. A nonlinear dynamical perspective on model error: A proposal for non-local stochastic-dynamic parametrization in weather and climate prediction models. *Quarterly Journal of the Royal Meteorological Society*, 127(572):279–304, 2001.
- [55] James C Robinson. *Infinite-dimensional dynamical systems: an introduction to dissipative parabolic PDEs and the theory of global attractors*, volume 28. Cambridge University Press, 2001.
- [56] GI Sivashinsky. Nonlinear analysis of hydrodynamic instability in laminar flames. derivation of basic equations. *Acta astronautica*, 4(11):1177–1206, 1977.
- [57] GI Sivashinsky and DM Michelson. On irregular wavy flow of a liquid film down a vertical plane. *Progress of Theoretical Physics*, 63:2112–2114, 1980.
- [58] Yiorgos S Smyrlis and Demetrios T Papageorgiou. Computational study of the kuramoto-sivashinsky equation. *Advances in Multi-Fluid Flows*, 86:426, 1996.
- [59] Roger Temam. *Infinite-dimensional dynamical systems in mechanics and physics*, volume 68. Springer Science & Business Media, 2012.

- [60] Michael K Tippett, Jeffrey L Anderson, Craig H Bishop, Thomas M Hamill, and Jeffrey S Whitaker. Ensemble square root filters. *Monthly Weather Review*, 131(7):1485–1490, 2003.
- [61] Xuguang Wang and Craig H Bishop. A comparison of breeding and ensemble transform kalman filter ensemble forecast schemes. *Journal of the atmospheric sciences*, 60(9):1140–1158, 2003.
- [62] Jeffrey S Whitaker and Thomas M Hamill. Ensemble data assimilation without perturbed observations. *Monthly Weather Review*, 130(7):1913–1924, 2002.
- [63] Jeffrey S Whitaker and Thomas M Hamill. Evaluating methods to account for system errors in ensemble data assimilation. *Monthly Weather Review*, 140(9):3078–3089, 2012.
- [64] John Worden and John Harvey. An evolving synoptic magnetic flux map and implications for the distribution of photospheric magnetic flux. *Solar Physics*, 195(2):247–268, 2000.
- [65] Yue Ying and Fuqing Zhang. An adaptive covariance relaxation method for ensemble data assimilation. *Quarterly Journal of the Royal Meteorological Society*, 2015.